Flood modelling with HydraTE[☆]: 2+1-dimensional smoothed-particle hydrodynamics

Peter A. Thomas[a], Frazer R. Pearce[b]

[a]*Department of Physics & Astronomy, University of Sussex, Brighton, BN1 9QH, UK*
[b]*School of Physics & Astronomy, University of Nottingham, Nottingham, NG7 2RD, UK*

Abstract

We present HydraTE, our own implementation of the smoothed-particle hydrodynamics technique for shallow water that uses the adaptive size of the smoothing kernel as a proxy for the local water depth. We derive the equations of motion for this approach from the Lagrangian before demonstrating that we can model the depth of water in a trough, implement vertical walls, recover the correct acceleration and terminal velocity for water flowing down a slope and obtain a stable hydraulic jump with the correct jump condition. We demonstrate that HydraTE performs well on two of the UK Environment Agency flood modelling benchmark tests. Benchmark EA3 involves flow down an incline into a double dip depression and studies the amount of water that reaches the second dip. Our results are in agreement with those of the other codes that have attempted this test. Benchmark EA6 is a dam break into a horizontal channel containing a building. HydraTE again produces results that are in good agreement with the other methods and the experimetal validation data except where the vertical velocity structure of the flow is expected to be multi-valued, such as the hydralic jump where the precise location is not recovered even though the pre- and post- jump water heights are. We conclude that HydraTE is suitable for a wide range of flood modelling problems as it preforms at least as well as the best available commercial alternatives for the problems we have tested.

Keywords: Smoothed Particle Hydrodynamics, Shallow water, Dam break, Flood, Mesh-free, Particle

[☆]Hydra for The Environment.

Email address: p.a.thomas@sussex.ac.uk (Peter A. Thomas)

1. Introduction

The modelling of water inundation has become a key tool for the assessment of the risk of flooding. The likely effect of costly physical interventions such as retaining walls and channel alteration can also be studied computationally. Given the increase in abnormal weather events such as localised heavy rainfall and the associated flash behaviour of downstream water catchments flooding events are likely to become more common. Reservoirs and other containment structures or bypass channels are also put under increased stress by these events and the possibility of failure should be considered and assessed. Given the very high cost of any physical intervention measure it is important that firm confidence in the modelling accuracy needs to be achieved. This is greatly aided by using a wide range of computational algorithm which hopefully converge on an agreed result. These algorithms need to be both verified and physically validated.

The Lagrangian particle method, smoothed-particle hydrodynamics (SPH) has an established ability to handle complex geometry whilst automatically conserving both mass and momentum. As such it is well suited to the problem of inundation. While the SPH algorithm itself was developed in the late 70's within astrophysics [1, 2] it has recently been used extensively within engineering for a variety of hydrodynamical problems including the inertial driven flows typically found in flooding scenarios. The application of SPH to shallow-water problems was proposed by Rodriguez-Paz and Bonet [3] who also demonstrated that their implementation passed some basic tests which were extended by Panizzo et al. [4]. More recently, the shallow-water or depth-average version of SPH has been applied to (for example); coastal flows [5], dam breaks [6, 7] and landslides [8]. The basic formulation has also been extended to include a better treatment of boundaries [9], allow for particle splitting and merging [10, 11] and better handling of discontinuities in the water bed [12] as well as being implemented on a GPU system [13].

In this report we introduce our own version of depth-averaged SPH. In Section 2 we present our algorithm. In Section 3 we show that our method performs well on four basic tests and introduce our implementation of boundary walls and damping of small scale power. In Section 4 we demonstrate that our method can undertake two of the standard tests from the UK Environment Agency Flood-modelling Benchmark Report [14]. We present a

summary in Section 5.

2. The HydraTE algorithm

The derivation of the equations in this section mostly follows that of Rodriguez-Paz and Bonet [3] except that we are more explicit in the derivation of the correction factor for spatially-varying smoothing lengths.

2.1. Basics

While we are chiefly interested in water, the smoothed-particle hydrodynamics (SPH) algorithm that we develop below can be applied to any incompressible liquid. Within SPH, the properties of the liquid are defined by the masses, m_i, positions $\boldsymbol{r}_i$ and velocities $\boldsymbol{v}_i$ of a set of particles, $i = 1 \dots N$, that represent Lagrangian fluid elements.

An estimate for the fluid properties at position $\boldsymbol{r}_i$ is obtained by averaging over neighbouring particle properties, using a weighting function, $W_{ij} = \mathcal{W}(|\boldsymbol{r}_j - \boldsymbol{r}_i|/h_i)/h_i^2$ (also known as a smoothing kernel) that is centred on $\boldsymbol{r_i}$ and has a characteristic smoothing length h_i. We use a kernel with compact support such that $\mathcal{W} = 0$ for separations greater than h_i, as described in Appendix A. In the general form of SPH the smoothing length, h_i, is variable and non-uniform across the simulation volume. Note the use of h_i in the argument of the kernel; it is important for the derivation of the equations of motion that W_{ij} is independent of h_j, the smoothing length of the neighbouring particle.

The essential key to our algorithm is that the particle separations (and therefore smoothing lengths) are not constant, as is typically enforced for SPH water algorithms, neither are they related to the local density. Instead we enforce an incompressible medium and use the smoothing length to indicate the depth of the local water column. In other words, the smoothing lengths are adjusted so as to always enclose the same mass of water, $M_{\rm SPH}$. Throughout this paper, we employ equal mass particles, $m_i = m$, so that the number of particles within the smoothing radius is fixed at $N_{\rm SPH} = M_{\rm SPH}/m$. This can be expressed by the constraints:

$$\phi_i \equiv \pi h_i^2 \sigma_i - M_{\rm SPH} = 0 \tag{1}$$

where the surface density of the water, σ, is proportional to the water depth and varies in inverse proportion to the square of h. Evaluating at the particle

locations, then

$$\sigma_i = \sum_j m_j W_{ij}. \tag{2}$$

Note: Equations 1 & 2 form a coupled set of equations for h_i & σ_i. Unlike previous implementations, we do not iterate to find exact values, but instead replace Equation 1 with the approximation

$$\phi \cong \sum_j m_j \tilde{W}_{ij} - M_{\rm SPH} = 0, \tag{3}$$

where $\tilde{W}_{ij}$ is unity if the separation of particles i and i is less than h_i and zero otherwise. This is quick to calculate, stable, and gives solutions that are almost indistinguishable from the original.

2.2. Shallow slopes

In order to keep the algebra simple and easy to follow, we first derive the equations of motion making the approximation that the vertical component of kinetic energy is much less than the horizontal one, i.e. that the slope of the surface on which the fluid sits is small. In the next section we will generalise to larger slopes.

Our derivation of the equations of motion then follows the procedure set out in Springel and Hernquist [15]. We start with a Lagrangian

$$\mathcal{L}(\boldsymbol{q}, \dot{\boldsymbol{q}}) = \sum_i \frac{1}{2} m_i \dot{\boldsymbol{r}}_i^2 - \sum_i m_i g \, (f_i + \frac{1}{2} d_i). \tag{4}$$

Here $\boldsymbol{q} = \{\boldsymbol{r}_i, h_i;\ i = 1 \ldots N\}$ are the independent variables; $f_i(\boldsymbol{r}_i)$ is the height of the floor at the location $\boldsymbol{r}_i$; and $d_i = \sigma_i/\rho$ is the depth of the fluid column, where ρ is the (constant) 3-dimensional mass density of the fluid.

The equations of motion are:

$$\frac{\mathrm{d}}{\mathrm{d}t}\left(\frac{\partial \mathcal{L}}{\partial \dot{q}_i}\right) - \frac{\partial \mathcal{L}}{\partial q_i} = \sum_{j=1}^{N} \lambda_j \frac{\partial \phi_j}{\partial q_i}, \tag{5}$$

where the λ_j are constants to be determined.

Taking $q_i = h_i$ gives

$$\frac{g}{2\rho} \, m_i \, \frac{\partial \sigma_i}{\partial h_i} = \sum_j \lambda_j \frac{\partial}{\partial h_i} (\pi h_j^2 \sigma_j). \tag{6}$$

This can be expanded and re-arranged to give

$$\lambda_i = \frac{g}{2\rho}\,\frac{m_i}{\pi h_i^2}\,\left[1 + \frac{2\sigma_i}{h_i}\left(\frac{\partial \sigma_i}{\partial h_i}\right)^{-1}\right]^{-1}. \tag{7}$$

Next, taking $q_i = \boldsymbol{r}_i$, we obtain

$$m_i \ddot{\boldsymbol{r}}_i + m_i g\,\frac{\mathrm{d}f_i}{\mathrm{d}\boldsymbol{r}_i} + \frac{g}{2\rho}\,\sum_j m_j\,\frac{\partial \sigma_j}{\partial \boldsymbol{r}_i} = \sum_j \lambda_j \pi h_j^2\,\frac{\partial \sigma_j}{\partial \boldsymbol{r}_i}; \tag{8}$$

$$m_i \ddot{\boldsymbol{r}}_i + m_i g\,\boldsymbol{s}_i + \frac{g}{2\rho}\,\sum_j m_j\,\mu_j \frac{\partial \sigma_j}{\partial \boldsymbol{r}_i} = 0, \tag{9}$$

where $\boldsymbol{s}_i = \boldsymbol{\nabla} f_i$ is the slope of the floor and

$$\mu_j = \left[1 + \frac{h_j}{2\sigma_j}\,\frac{\partial \sigma_j}{\partial h_j}\right]^{-1}. \tag{10}$$

Expressing the result in terms of the smoothing kernel gives

$$\ddot{\boldsymbol{r}}_i + g\,\boldsymbol{s}_i + \frac{g}{2\rho}\,\sum_j m_j \left[\mu_j\,\frac{\partial W_{ji}}{\partial \boldsymbol{r}_i} + \mu_i\,\frac{\partial W_{ij}}{\partial \boldsymbol{r}_i}\right] = 0 \tag{11}$$

and

$$\mu_i = -\frac{2h_i \sum_j m_j \mathcal{W}_{ij}}{\sum_j m_j \mathcal{W}'_{ij} r_{ij}}, \tag{12}$$

where $\mathcal{W}'_{ij}$ is the derivative of $\mathcal{W}_{ij}$ and $r_{ij} = |\boldsymbol{r}_j - \boldsymbol{r}_i|$. Finally, use the approximate symmetry of W_{ij} and W_{ji} to write

$$\ddot{\boldsymbol{r}}_i + g\,\boldsymbol{s}_i + \frac{g}{2\rho}\,\sum_j m_j \left[-\mu_j\,\frac{\partial W_{ij}}{\partial \boldsymbol{r}_j} + \mu_i\,\frac{\partial W_{ij}}{\partial \boldsymbol{r}_i}\right] \approx 0. \tag{13}$$

Note:

- This last step is not exact because the derivatives $\partial W_{ij}/\partial \boldsymbol{r}_i$ and $\partial W_{ji}/\partial \boldsymbol{r}_j$ use different values for the smoothing kernel and so do not exactly sum to zero.
- The expression for the inter-particle force is symmetric in i and j which means that momentum is conserved. In the absence of dissipation, as here, the force is directed along the line joining each pair of particles and so angular momentum is also conserved.

- In practice, we find that whether or not the μ_i term is included makes little difference to any of the flows that we study here, including those with abrupt changes in h_i such as a hydraulic jump. This is in contrast to 3-D astrophysical flows in regions with strong density gradients where the μ_i term can be important.

Our final equation of motion for shallow slopes is therefore

$$\ddot{\boldsymbol{r}}_i = \boldsymbol{t}_i - g\,\boldsymbol{s}_i, \tag{14}$$

where

$$\boldsymbol{t}_i = \frac{g}{2\rho}\sum_j m_j \left[\mu_j \frac{\partial W_{ij}}{\partial \boldsymbol{r}_j} - \mu_i \frac{\partial W_{ij}}{\partial \boldsymbol{r}_i}\right]. \tag{15}$$

2.3. Arbitrary slopes

When the slope of the floor is not restricted to be small then we need to include a vertical component of kinetic energy:

$$\mathcal{L}(\boldsymbol{q}, \dot{\boldsymbol{q}}) = \sum_i \frac{1}{2} m_i (\dot{\boldsymbol{r}}_i^2 + (\dot{\boldsymbol{r}}_i.\boldsymbol{s}_i)^2) - \sum_i m_i g\,(f_i + \frac{1}{2} d_i). \tag{16}$$

Extra terms then appear in the equations of motion:

$$\ddot{\boldsymbol{r}}_i + (\ddot{\boldsymbol{r}}_i.\boldsymbol{s}_i)\boldsymbol{s}_i + (\dot{\boldsymbol{r}}_i.\dot{\boldsymbol{s}}_i)\boldsymbol{s}_i + (\dot{\boldsymbol{r}}_i.\boldsymbol{s}_i)\dot{\boldsymbol{s}}_i - (\dot{\boldsymbol{r}}_i.\boldsymbol{s}_i)(\dot{\boldsymbol{r}}_i.\boldsymbol{\nabla})\boldsymbol{s}_i + g\,\boldsymbol{s}_i - \boldsymbol{t}_i = 0. \tag{17}$$

Now, assuming that the floor height is not time-dependent, then $\dot{\boldsymbol{s}}_i = (\dot{\boldsymbol{r}}_i.\boldsymbol{\nabla})\boldsymbol{s}_i$ and the above expression simplifies to

$$\ddot{\boldsymbol{r}}_i + (\ddot{\boldsymbol{r}}_i.\boldsymbol{s}_i)\boldsymbol{s}_i + \dot{\boldsymbol{r}}_i.\boldsymbol{\kappa}_i.\dot{\boldsymbol{r}}_i + g\,\boldsymbol{s}_i - \boldsymbol{t}_i = 0, \tag{18}$$

where $\boldsymbol{\kappa}_i = \boldsymbol{\nabla}\boldsymbol{s}_i = \boldsymbol{\nabla}\boldsymbol{\nabla}\boldsymbol{f}_i$. The second term in this equation represents a correction due to the fact that the motion is not in the horizontal plane; the third comes from the curvature of the surface; and the fourth from the component of gravity acting along the surface.

Equation 18 can be rearranged to give

$$\ddot{\boldsymbol{r}}_i = \boldsymbol{t}_i - \frac{\dot{\boldsymbol{r}}_i.\boldsymbol{\kappa}_i.\dot{\boldsymbol{r}}_i + g + \boldsymbol{t}_i.\boldsymbol{s}_i}{1 + s_i^2}\boldsymbol{s}_i. \tag{19}$$

Note: In principal the vertical kinetic energy should also include a component from the changing depth of the fluid, but this will usually be small except in shocks. It gives rise to force terms that involve second derivatives and so are subject to numerical noise, and therefore we choose to neglect it.

2.4. Extras

In addition to the basic algorithm described above, we need to introduce extra forces to prevent penetration of particles into walls, and to damp fluctuations on scales smaller than the smoothing kernel. These are described in detail in Appendix B and Appendix C, respectively.

3. Basic test cases

3.1. Case 1: a static trough of water with sloping sides

We study the behaviour of water in a horizontal triangular trough of depth $d = |x|$ with periodic boundary conditions in the y-direction at $y = 0$, 1. We insert 1024 water particles, a number deliberately kept small so as to show up any deficiencies clearly. The uniform mass of the individual particles is chosen so that the expected volume is 1: thus the expected height of the water surface is also 1. The upper panel of Figure 1 shows the particle locations viewed from above the trough once all motion has essentially stopped. The middle panel shows the depth profile of the trough viewed from the end. The lower panel indicates the height of the water surface recovered by each of our particles as a function of their x-position. Vertical dashed lines indicate the effective size, h, of the SPH particles at the centre and the edges of the distribution. Due to this smoothing the position of the water surface near the centre of the trough is not well recovered because the slope is not constant about this point. Rather, all the adjacent particles are in a shallower part of the trough and so the recovered surface will be consistently underestimated. The curved line indicates the surface once this effect has been taken into account.

The first thing to note is that the particle distribution is not completely disordered. This is because for SPH the particles tend to spread out roughly uniformly, and over time will settle into a 'glass'-like pattern with small-scale order (but not, in general, long-range order). In this particular case, because of the symmetry imposed by the ridge-line at $x = 0$ and the edges at $|x| = 1$, an obvious linear pattern does emerge at those locations. Note that, as expected for our method where the mass of a particle is uniform and the size is a proxy for the water depth, the separation of the particles varies with distance from the centreline of the trough. The vertical dashed lines in the figure show the extent of the smoothing kernels for particles located at the left- and right-hand edges of the distribution and at $x = 0$. One consequence of this size gradient is that the particle distribution is uneven across the

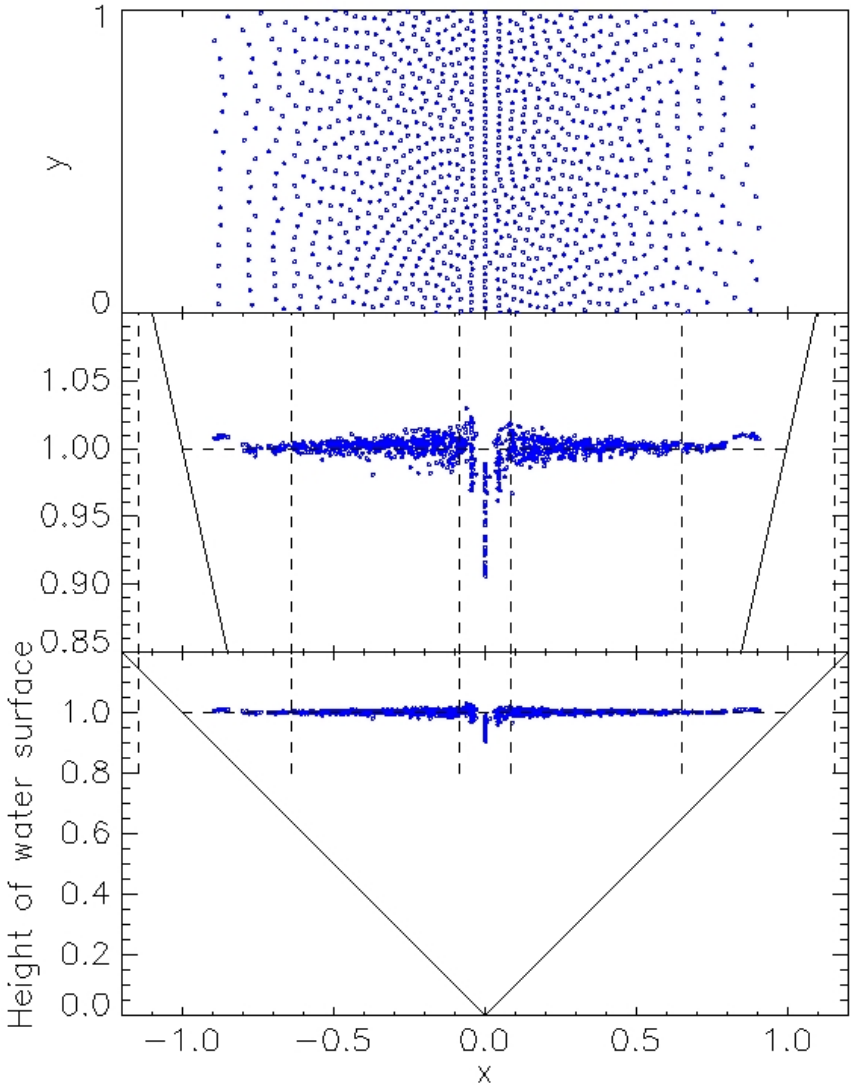

Figure 1: Upper panel: a map of the particle locations in the case 1 trough, as described in the text. Middle and lower panels: the profile along the x-direction of the depth of water in the trough at the location of each particle. The three pairs of vertical dashed lines indicate the extent of the smoothing kernels for particles located at the left- and right-hand edges of the distribution and at $x = 0$. The lower panel is drawn to scale; the middle panel has had its y-scale exaggerated to highlight the measurement errors.

smoothing kernel, with the majority of a particle's neighbours on the side nearer the centreline: for particles on the extreme edges of the distribution, all their neighbours lie on the side closer to the centre.

Given that for this test we are smoothing over just 24 neighbours the recovered surface height is generally remarkably accurate everywhere except near the ridge-line at $x = 0$. It is not surprising that the depth is underestimated near the centreline because the floor rises on both sides of the particle location. Essentially the gradient of the floor is changing on a scale much smaller than the size of the smoothing kernel. A more accurate result could be obtained if required by increasing the particle number and therefore the effective resolution of the model, allowing the sharp slope change to be better resolved.

In regions where the particle kernel extends only over a uniform gradient of floor-height there is very little bias in the density estimate and the root-mean-square scatter in the height of the water surface is 0.005. A very slight over-estimate of the height occurs near the edges of the distribution, but this has a magnitude of less than 1 per cent.

3.2. Case 2: a static pond of water with vertical walls

We next consider the situation of an 'L'-shaped pool of water surrounded by vertical walls. Such a pool has 6 straight walls, close to which a particle's smoothing kernel will be only half full, joined at right angles at 5 'outer' corners near which the kernel will be only one-quarter full and one 'inner' corner where the kernel is three-quarters full. For vertical walls the gradient of the slope of the floor is formally infinite, and so we need some other way of confining the water. Particles at a distance b from a wall, where $b < h$, will be missing neighbours and hence will have a reduced repulsive force, causing them to be accelerated towards the wall. There are many methods of compensating for this (e.g. the introduction of ghost particles on the far side of the wall or a chain of repulsive wall particles) which can here run into difficulties because our method perforce involves a variable sized smoothing kernel, h, and therefore range at which any wall becomes visible to a particular particle. To allow for this the method we adopt here is to add an additional repulsive force to replace that which would have been expected in a uniform, static distribution. The details of our method are described in Appendix B.

As shown in Figure 2 our wall correction does an excellent job along the edges of the pond, and a very good one at the interior corner. It does slightly

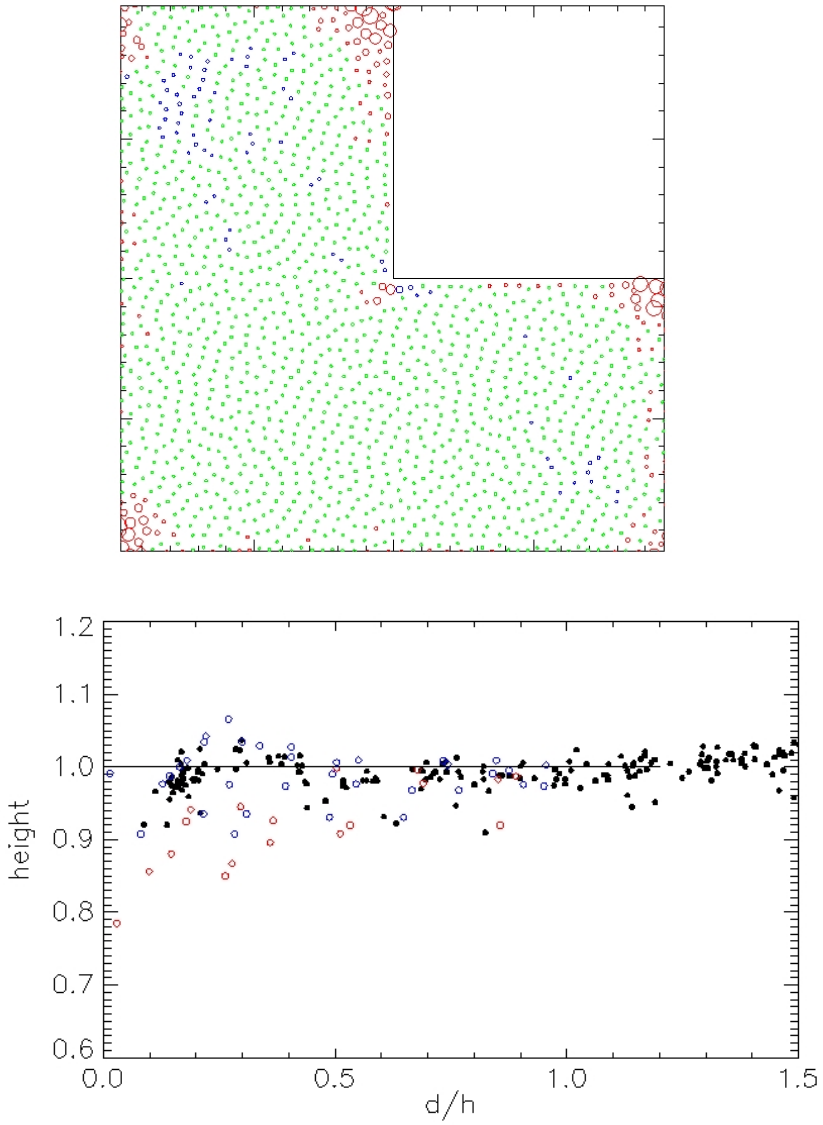

Figure 2: Top panel: a map of the particle locations in a pond with vertical walls, as described in the text. The red colouring refers to heights below 0.975 and the blue to heights above 1.025, with the size of the symbols reflecting the magnitude of the deviation from unit height. Bottom panel: a plot of height versus distance from the wall in units of the smoothing length, for a selection of particles. The red symbols are particle near the outer corners while the blue symbols are particles near the inner corner.

less well at the outer corners where particles occupy only one quadrant. This deviation is systematic and so it would be possible to correct for it in future work, but we do not do that here.

3.3. Case 3: unconfined flow down a slope with Manning drag

For our third test case we follow the flow of water down a uniform inclined plane of slope s. We employ periodic boundary conditions in both directions. With a Manning's drag coefficient of $\mathcal{D}$, the terminal speed of the flow should be

$$v_{\text{terminal}} = \frac{d^{\frac{2}{3}} s^{\frac{1}{2}}}{C_{\text{Manning}}}, \tag{20}$$

where d is the water depth and C_{Manning} is the Manning coefficient.[1] If the water starts from rest, then the time-evolution of the speed is

$$v(t) = v_{\text{terminal}} \tanh(t/\tau), \tag{21}$$

where $\tau = gs/C_{\text{Manning}}$ and g is the acceleration due to gravity.

Without any damping the scatter in the speed of individual particles grows uncontrollably with time. To counteract this we introduce various degrees of damping, detailed in Appendix C, all of which gave similar results provided that the damping coefficient was large enough. We fixed upon a choice of linear damping with $C_{\text{damp}} = 3$ although quadratic damping with $C_{\text{damp}} = 1$ gave very similar results.

The left panel of Figure 3 shows that the average water speed grows in very good agreement with Equation 21. In fact, the maximum deviation from the predicted relation occurs early on and is just 0.6 percent. The right panel shows that the scatter in the speed of individual particles has reduces greatly as the simulation progresses, and in fact it is just 0.3% by time $t = 300\,\text{s}$.

3.4. Case 4: a standing hydraulic jump

In case 4 we test the code's ability to handle strong discontinuities in height, such as occur in an hydraulic jump. We set up a long channel of water with periodic boundaries in the y-direction and a hydraulic jump at $x = 0$. For water depths on the left and right of the discontinuity of d and

[1] We note that the water depth should be measured perpendicular to the surface, and the flow-speed parallel to the surface. Where the slope is small, as here, this would make only a small correction. We intend to implement this in future work.

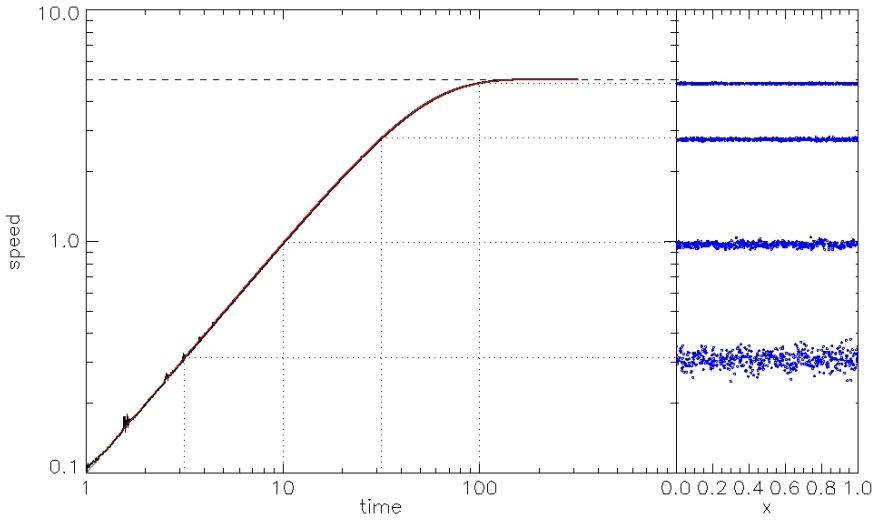

Figure 3: Left panel: The time evolution of the mean speed of the water flow in the Manning drag test. The measured speed in black is over-plotted in red by the theoretical relation from Equation 21 – the two are almost identical. Right panel: the speeds of individual SPH particles in a small portion of the flow at 5 different times, as indicated.

$2d$, respectively, we require an inflow speed at $x < 0$ of $v_- = (3gd)^{1/2}$, where g is the acceleration due to gravity. In this test, we take $d = 1$.

The upper panel of Figure 4 displays the distribution of the particles at time $t = 10/v_-$, by which time particles that started at $x = -10$ should just have reached the jump. Particles that originated between $-10 < x < -9$ are coloured red; others are blue. This illustrates two things: firstly, the flow has progressed at the correct speed, with no sign of drifting from the original location at $x = 0$ – a non-trivial result given the Lagrangian nature of the code; secondly, there is very little interpenetration, or mixing, of particles as they pass through the jump.

The lower panel of Figure 4 shows a profile of the height variation across the jump, which agrees very closely with the theoretical prediction. The ringing that is seen just downstream of the jump has a wavelength which is of order the smoothing length of the particles (illustrated by the short vertical lines) and is a consequence of the finite resolution of the simulation.

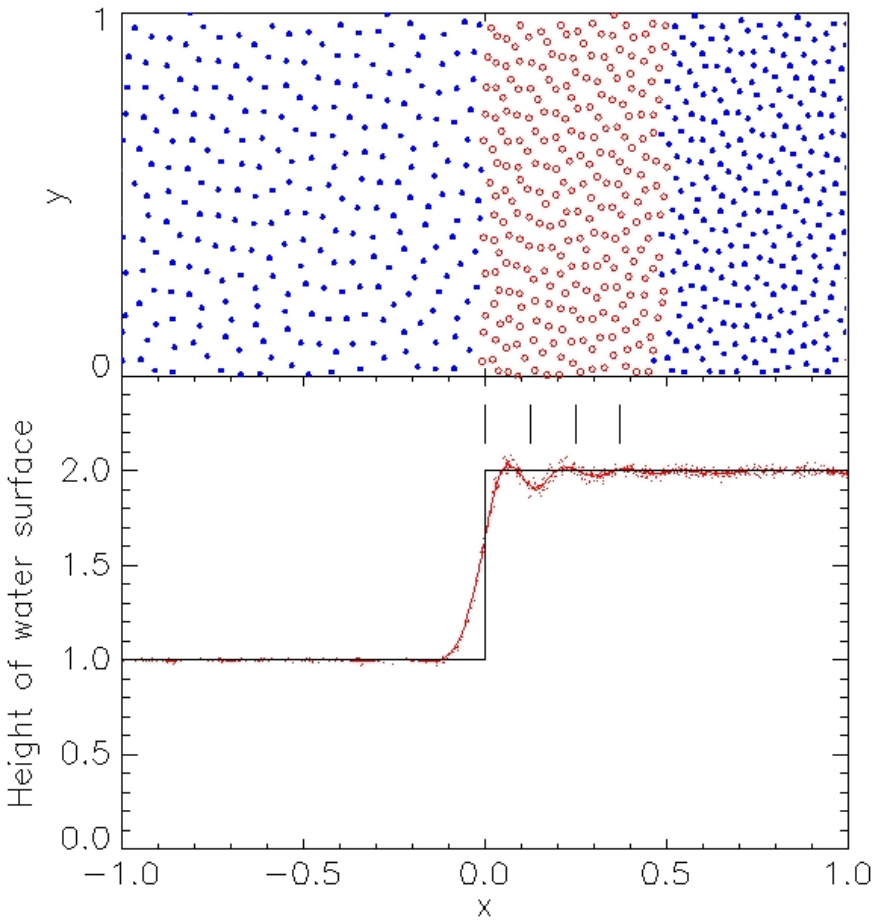

Figure 4: Upper panel: a map of the particle locations in an hydraulic jump, as described in the text. Red points indicate particles that should have recently transited the jump at this time. Lower panel: the profile along the x-direction of the depth of water across the jump. The points show the height estimated at the location of each particle. The solid red line (hard to see except at the jump itself) shows the density smoothed over 17-particles in the x-direction. The solid back line shows the expected height variation across an idealised jump. The short vertical black lines are separated by one smoothing length in the high-density region.

4. UK Environment Agency benchmarks

We reproduce two of the UK Environment Agency water flow benchmark tests [14]. The first, EA3, is a relatively straightforward momentum con-

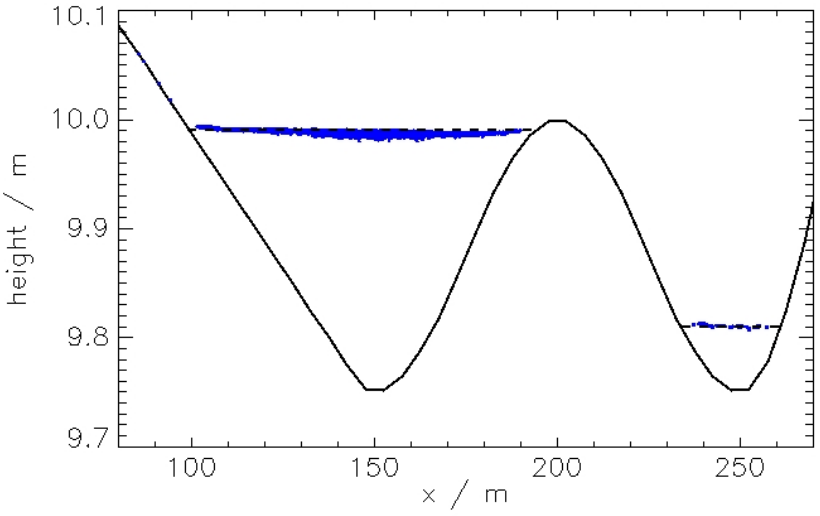

Figure 5: A profile showing the slope of the floor in the x-direction in test EA3 (note that the vertical and horizontal scales are very different), with the blue points showing the water level at the end of the test.

servation test with smoothly sloping walls and laminar flow. The second, EA6, is a much harder dam emptying test which includes vertical walls and hydraulic jumps.

4.1. EA3: momentum-driven flow down a slope into a double dip

Test EA3 represents the flow of water down a slope into a double dip separated by a small hump. Published results obtained using a variety of different hydrodynamical methods indicate quite a range in the amount of water that flows over the hump into the second dip. The flow over the hump is described as 'momentum-driven' in that the flow down the slope from the initial inlet location imparts momentum that carries the water over the hump. The test specifies the volumetric flux of water passing $x = 0\,\mathrm{m}$ as a function of time between $t = 5\,\mathrm{s}$ and $t = 35\,\mathrm{s}$, but does not specify what the momentum of the water is at that time. A pictorial representation of the inflow is shown in Figure D.11 in Appendix D.

Figure 5 shows a cross-section through the floor-level in the x-direction (there is no slope in the y-direction, which has a width of 100 m). Also shown on the right, by the blue points, is the water level after 900 s have elapsed, which is specified as the end of the test. The gradient of the slope has been

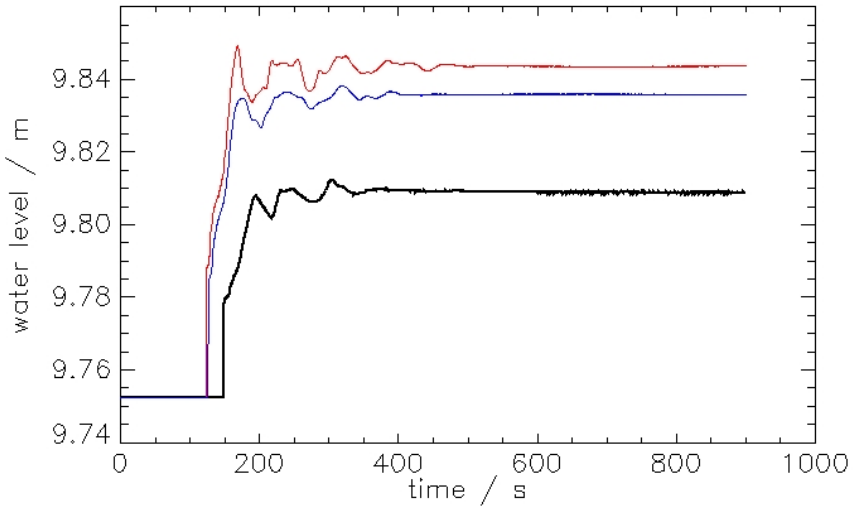

Figure 6: Test EA3: the height of the water column at $x = 250\,\mathrm{m}$ as a function of time. Red - water enters with momentum; Blue - water has its x-momentum set to zero as it crosses the $x = 0$ boundary; Black - as for the blue curve but in addition all particles within the region $x/\mathrm{m} = [0, 5]$ have their velocity set to the mean velocity of particles in this region every time-step.

greatly exaggerated in this plot as the vertical and horizontal scales are very different.

Due to the ambiguity in the momentum of the inflowing water, we show in Figure 6 three different measurements of the water depth at the specified location, $x = 250\,\mathrm{m}$ as a function of time. For the upper, red, curve the water enters with a speed, v_x, equal to the terminal speed for flow down a slope of this gradient at the specified volumetric flux of $62.5\,\mathrm{m^3 s^{-1}}$ and Manning coefficient: $v_x \approx 2.74\,\mathrm{ms^{-1}}$. For the middle, blue, curve the inflow velocity, v_x, is set equal to zero. These two span the plausible range of inflow speeds and yet both give final water depths in the second dip that are significantly greater than every one of the twelve codes that participated in the EA test. However, the lower, black, curve shows that we can recover the previous results if we modify our initial conditions to more closely mimic those of a grid code by essentially assuming the zero velocity inlet is at the midpoint of the first grid cell rather than at $x = 0$.

The EA test specified that the grid-cells employed should have a width of $5\,\mathrm{m}$, a specification that is not applicable for our method which is fully

Lagrangian. However, we can attempt to replicate the behaviour of a grid code near the inlet by forcing all the particles in the first 5 m to move with the same velocity. To conserve momentum, this velocity is set to the mean of the particles in the region. The black curve shows the results of such a test, with the inflow speed, v_x, again set to zero. The variation seen in Figure 6 indicates that this test is not particularly well posed as the results are very sensitive to the precise definition of the initial conditions which are not completely specified.

The majority of test-participants gave final water surface levels at the measurement point within the second dip in the range 9.805-9.830 m, so we are fully consistent with these results. Our water depth has settled down into a steady state after 300 s, earlier than for most other codes, indicating that for us any sloshing behaviour rapidly damps away (although, as can be seen in Figure 5, sloshing continues in the deeper dip). Without knowing the correct experimental solution to the problem, which as far as we are aware has never been published, it is not clear whether this is a good or a bad thing.

We present the other results from the test (the water depth at $x = 150$ m, plus the water speed at $x = 150$ & 250 m) in Appendix D. Here we also show the effect of changing the damping scheme that we use: while this can alter the detailed time-evolution of the solution it does not affect the final water level in the second dip.

4.2. EA6: a dam-break with an obstacle

The objective of the test is to assess the ability to simulate hydraulic jumps and wake zones behind buildings using high-resolution modelling. The geometry of the problem is illustrated in Figure 7, which shows a snapshot of the flow at time $t = 7$ s.[2]

The lay-out of this test is that of a water filled dam with an attached horizontal outflow channel that contains an obstruction. At the start the water depth within the dam is 0.4 m and the outflow channel is uniformly filled to a depth of 0.02 m. The water is confined to the flat bed of the channel by gently sloping sides that start to rise from $|y| = 1.34$ m and vertical walls at $|y| = 1.8$ m. There are also vertical end walls at $x = -7.55$ m and $x = 91.45$ m. Within the channel there is a building, represented by a

[2] A movie of the flow can be viewed at `https://www.dropbox.com/s/1jssl5fj3jg2lkc/ea6_map.avi`

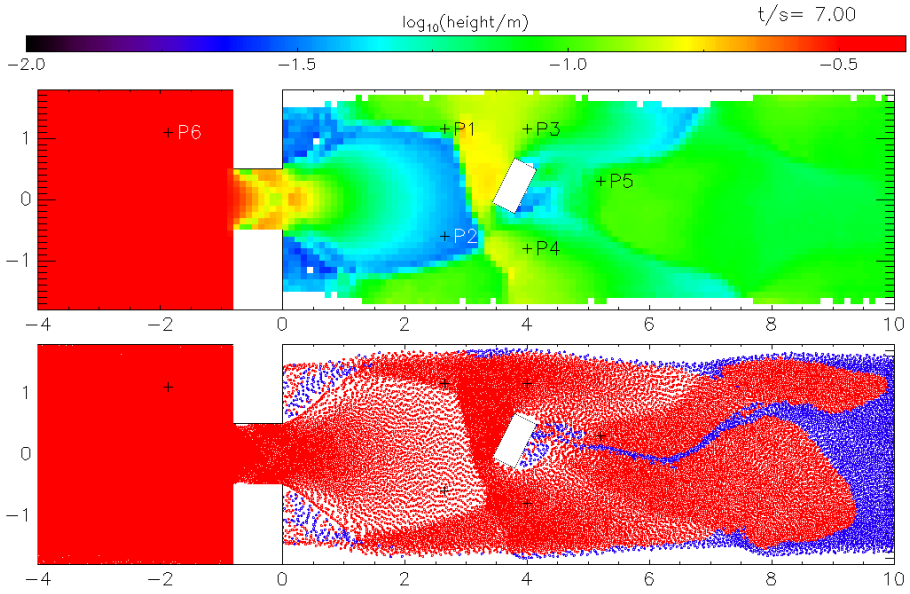

Figure 7: Test EA6: a map of the flow at time $t = 7\,\mathrm{s}$. The lower panel shows the particle distribution in our lowest-resolution run, and the upper panel the corresponding density in squares of side 0.5 m.

cuboidal obstruction placed at an angle, as shown. At time $t = 0\,\mathrm{s}$, the barrier at $x = 0\,\mathrm{m}$ is removed and the water is free to flow down the channel. Measurements of the water depth and the speed of the flow at 6 locations (marked with plus signs on the figure) were recorded using a physical model at the Civil Engineering Laboratory of the Universite Catholique de Louvain [16].

The test specification calls for a resolution element of $0.5\,\mathrm{m}\times0.5\,\mathrm{m}$, or 36 000 nodes in the simulation region. It is not obvious how to interpret this for our Lagrangian SPH code but recall that the SPH method smooths properties over a scale that corresponds to the smoothing kernel and that we have chosen this to encompass 24 particles. We therefore undertook simulations at three different resolutions: low, where the SPH kernel within the dam roughly covered one resolution element (i.e. there are approximately 24 particles per $0.5\,\mathrm{m}\times0.5\,\mathrm{m}$ within the dam) for a total of 118 286 particles; standard, where the SPH kernel averaged over the entire simulation volume roughly encompasses 24 particles, requiring 739 635 particles in total; high – as a test of convergence, 96 particles per element, averaged over the simulation volume, 2 959 236 particles in total.

The lower panel of Figure 7 shows the particle distribution in the low-resolution run at a time when a hydraulic jump has formed in front of the building. The red/blue colouring encodes particles that orginated at x/m less/greater than zero, respectively. As can be seen, some water has been trapped in stagnant regions behind the dam walls and the building. One of the advantages of SPH is that it avoids artifical mixing of the fluid and allows easy visualisation of these flow patterns.

To make the density field shown in the upper panel of Figure 7, we have averaged the density of particles within each resolution element. To some extent, this over-smooths the data, since the density at each particle location is already a kernel average over its neighbours, but we wished to produce a map that is directly comparable to that produced by grid codes. In subsequent plots we will show results at this same resolution for easy comparison.

In Figure 8 we compare the density in the three runs at time $t = 25\,\mathrm{s}$. The first thing to note is that the three are very similar. There is a little bit more detail as one moves to higher resolution, but the broad picture is the same. We have chosen this particular output time, however, to illustrate one particular feature, and that is that the location of the hydraulic jump in front of the building has shifted between the lowest and the two higher-resolution runs so that it lies on the other side of the measurement point, P2. This

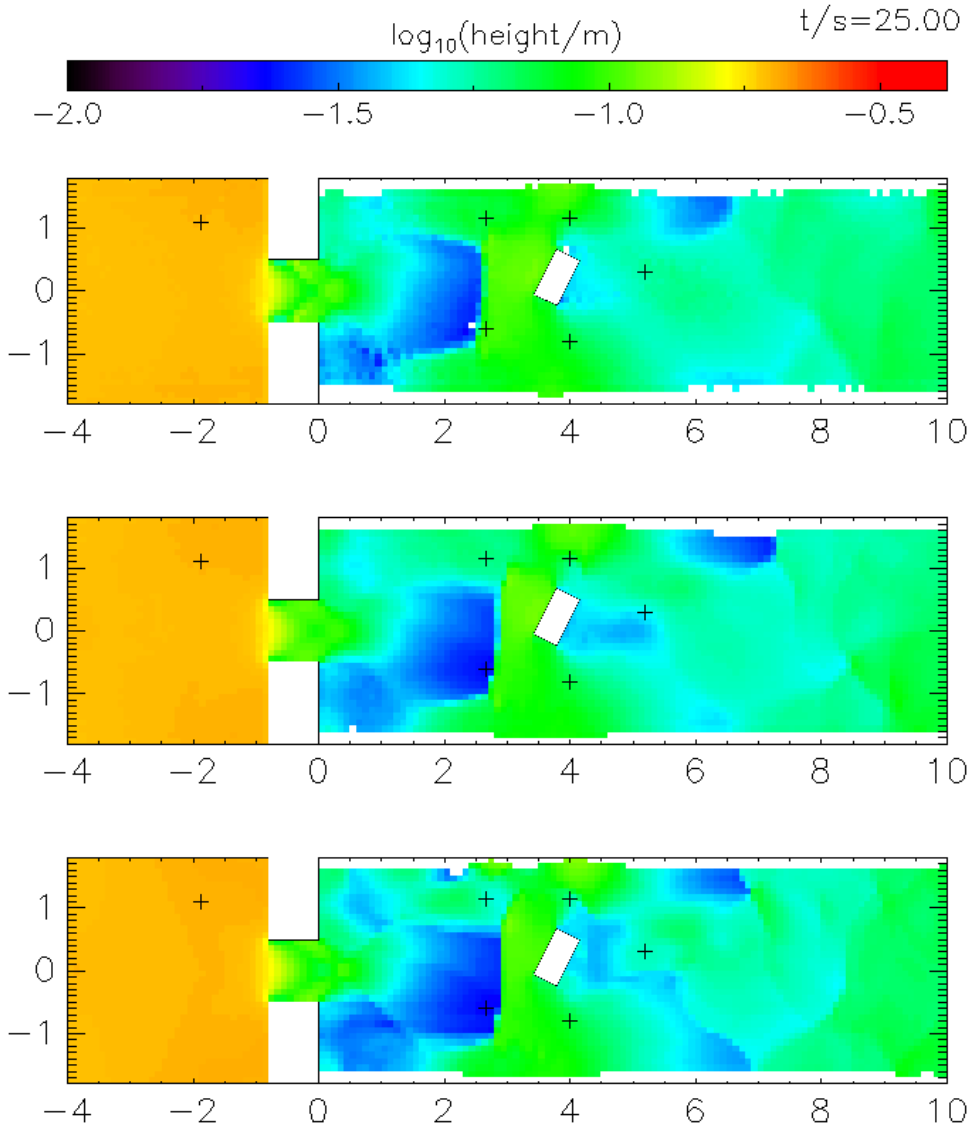

Figure 8: Test EA6: density maps of the flow at time $t = 25\,\mathrm{s}$. The upper, middle and lower panels correspond to the low-, standard- and high-resolution runs, respectively.

makes a huge difference to the temporal evolution of the measured height at that location, as shown in Figure 9.

The bottom panel of this figure shows the surface level for measurement point P6 within the dam. The water level here is very well converged between the three runs and very similar to the experimental result and those reported by other codes. The water does not leave the dam uniformly but rather demonstrates glugging behaviour, illustrated by the non-uniform rate of change of the level at P6. Results from measurement point P4 are shown in the middle panel of Figure 9. The results from points P1, P3 & P5 show a similar level of agreement between the three resolutions. Close but not perfect agreement is seen between the runs and the experimental data. Downstream of the obstruction the water level is converged and recovered well.

The upper panel of Figure 9 displays results for measurement point P2, upstream and below the obstruction, close to the location of the hydraulic jump. This jump is caused by the laminar outflow stream from the dam encountering the obstruction and stalling. In reality the vertical flow structure near this point will be multi-valued, with a deep, fast moving current flowing under an essentially static (and frequently highly aerated) upper layer that exhibits a gentle vertical recirculation. Such a vertical velocity structure cannot be followed by our method, or any other 2-D method that assumes that the vertical flow is single-valued. As such it is perhaps not surprising that the exact location of the hydraulic jump is poorly recovered. We note also that it is not clear where this hydraulic jump should be positioned in the real-world experiment either: precisely what is meant by 'water height' when the surface is highly aerated? This aeration may by behind the observed slow rise time in the experimental data for the water height at measurement point P2 in the published data that is a also not recovered by any of the other codes that have reported this test.

For our code, the water depth measurements at point P2 show very similar evolution up to $t = 18\,\mathrm{s}$, but beyond that the point P2 then gets overtaken by the hydraulic jump in the low-resolution run, whilst remaining outside it in the higher-resolution runs. Once the jump recedes back past P2 in the low-resolution run after $t \approx 35\,\mathrm{s}$ the three resolutions again give similar results. We take the close agreement between the standard and high-resolution runs to indicate numerical convergence: there is some finer detail visible at high resolution but not enough to justify the extra computational resource.

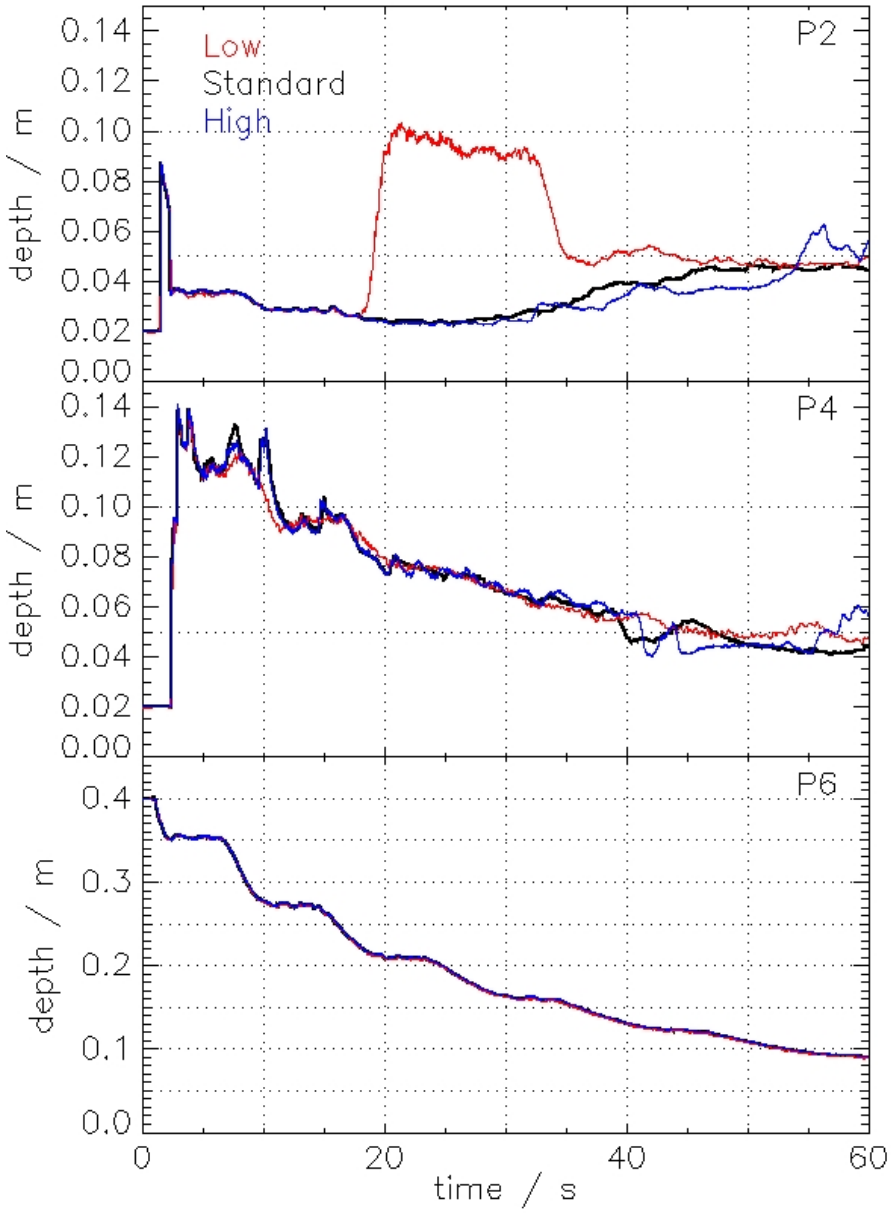

Figure 9: Test EA6: the time evolution of the water depth at three different locations, P2, P4 & P6, as shown in Figure 8. In each case the thin red, thick black and thin blue lines refer to the low, standard and high-resolution runs, repsectively.

5. Summary

In this report we introduced HydraTE, our implementation of the Lagrangian smoothed-particle hydrodynamics method that utilises the adaptive kernel smoothing of SPH as a proxy for the water height. This simple adaptation converts the three dimensional SPH into a two-plus-one dimensional method that is accurate for flooding problems where the flow is well described by a single-valued velocity.

After describing the method, we performed a series of simple case study tests of our approach, demonstrating that the method can recover the depth of water in a trough, the depth of water within a still pool with vertical walls, the speed of water flowing down a slope and the height of water crossing an hydraulic jump. For the trough, the method is very accurate except near the centreline where the curvature of the underlying surface is sharper than the scale on which the SPH kernel is smoothed. For the pool, the depth of the water near the walls is close to that desired except near the corners where the smoothing kernel is very far from being filled. We aim to improve our method of implementing vertical walls in future work. For water flowing down a slope, we recover both the acceleration and the terminal velocity of the flow very well by implementing a standard Manning coefficient. The method is also capable of recovering an hydraulic jump correctly without any drift of the jump location, an important test for a Lagrangian method. Typical post-jump ringing behaviour is observed, as expected, and these oscillations on the scale of the smoothing kernel rapidly damp away.

Once we have established that HydraTE passes the simple test cases we applied it to two of the UK Environment Agency benchmark flow tests, EA3 and EA6. These tests involve the flow of water down an incline into a double dip and a dam break into a horizontal channel containing a building. For EA3 we demonstrated that a similar amount of water could end up in the second dip as obtained by other simulation codes, if we interpreted the specified initial condition to mimic that of a grid code. The initial conditions of this test are poorly posed and there does not appear to be any experimental validation data available. The results obtained for our code are well within the range observed for other simulation methods and we conclude that it works at least as well as any other approach for this particular test. For EA6 the height measurements at five of the 6 measurement points are close to both the experimental validation data and the results of the other codes. At the final point, P2, this is not the case for our higher resolution runs. This

measurement point is situated near to the location of the hydraulic jump that marks where the laminar dam outflow interacts with the building placed in the channel. The recovered depth of the water here is therefore very sensitive to the location on the jump, which moves in time as the dam outflow rate changes in response to the changing water level in the dam. We note that the shape of the experimental validation data for this point is in fact very different to that of all the simulation codes reporting results, including ours, displaying a much less abrupt rise. The results here are in agreement with those presented for other implementations of shallow-water SPH on similar tests (see for example Figures 13 & 14 of Vacondio et al. [11]). All depth-averaged methods will naturally struggle here: in the real world the fast laminar outflow will penetrate under the location of the hydraulic which will exhibit a slow vertical circulation. Such vertical velocity structure cannot be accurately recovered by a shallow-water method, even it does recover both the pre- and post- jump water levels very accurately. We also note that in reality the water surface near to this hydraulic jump will be very turbulent and aerated so what precisely is meant by the 'surface' and how the location of this surface is experimentally measured is not at all clear. For this test HydraTE produces converged results on a scale where one resolution element is roughly matched by the size of the SPH smoothing kernel.

In conclusion, we have developed and implemented HydraTE, a shallow-water SPH method that has proved useful for a range of real-world water flow problems, producing verified results that are close to those obtained by the best currently available commercial techniques. The method has proved to be highly adaptable and applicable to a range of water flow problems where the vertical structure of the flow is not an important consideration. The two main advantages of the method are (i) explicit conservation of mass and momentum, and (ii) the Lagrangian nature meaning that computational resource is focussed on the regions of interest. This makes it a useful alternative to grid-based codes for a wide range of real-world problems.

Acknowledgements

PAT acknowledges support from the Science and Technology Facilities Council (grant number ST/I000976/1).

The authors contributed in the following ways to this paper: PAT developed the theory of 2+1-dimensional SPH and did most of the testing; FRP

& PAT co-developed the original HYDRA code on which it was based and co-authored the paper.

Former PDRA Chris Short and undergraduate project student Hon Mond Ng did considerable work on a 3-dimensional version of SPH whose limitations motivated development of the algorithm described in this paper. Undergraduate project student Cullan Howlett helped to develop the damping and short-range forces.

Appendix A. Smoothing kernels

The smoothing kernel is $W_{ij} = \mathcal{W}(|\boldsymbol{r}_j - \boldsymbol{r}_i|/h_i)/h_i^2$ where

$$\mathcal{W}(x) = \frac{40}{7\pi} \begin{cases} 1 - 6x^2 + 6x^3, & 0 \le x \le \frac{1}{2}; \\ 2(1-x)^3, & \frac{1}{2} < x \le 1; \\ 0, & x > 1. \end{cases} \tag{A.1}$$

Appendix B. Walls

Walls are specified in the code by endpoints $\boldsymbol{r}_{\mathrm{wall},1}$ and $\boldsymbol{r}_{\mathrm{wall},2}$, with the normal $\hat{\boldsymbol{n}}_{\mathrm{wall}} = \hat{\boldsymbol{z}} \wedge (\boldsymbol{r}_{\mathrm{wall},2} - \boldsymbol{r}_{\mathrm{wall},1})/|\boldsymbol{r}_{\mathrm{wall},2} - \boldsymbol{r}_{\mathrm{wall},1}|$ pointing away from the fluid. For a particle at location $\boldsymbol{r}_i$, empirical measurement gives a missing acceleration of

$$\boldsymbol{a}_{\mathrm{wall}} = -\hat{\boldsymbol{n}}_{\mathrm{wall}} \frac{\sigma}{h} \min\left(0, e^{\alpha(\beta - x)} - e^{\alpha(\beta-\gamma)}\right), \tag{B.1}$$

where x is the distance from the wall, $x = (\boldsymbol{r}_i - \boldsymbol{r}_{\mathrm{wall},1}).\hat{\boldsymbol{n}}_{\mathrm{wall}}$. The negative sign ensures that the acceleration acts into the fluid and we set $\alpha = 2.9, \beta = 1.1$ and $\gamma = 0.95$ We apply such a term only if the perpendicular line $\boldsymbol{r}_i + \lambda\hat{\boldsymbol{n}}_{\mathrm{wall}}$ (where λ is a free parameter) intersects the wall

In addition to the above, we allow particles to bounce elastically off the wall if their motion would take them across it over the course of the next timestep. In practice, because of the repulsive acceleration described above, this rarely happens.

Appendix C. Damping

In many situations water flows can be regarded as essentially dissipationless, and so we want to limit the extent to which we impose any artificial

viscosity into the simulation. Nevertheless, some viscosity is required in order to damp out fluctuations on scales smaller than the smoothing length that would otherwise lead to unnecessarily short timesteps.

Our approach is to impose a smooth variation in velocity across the smoothing kernel. We consider two possibilities: a linear, or a quadratic variation. In principle, the latter is preferable as it permits a higher order variation across the kernel, but in practice we find that it makes little discernible difference.

Consider a particle i at location $\boldsymbol{r}_i$. Suppose that each component of the underlying velocity field varies quadratically with $(x, y) = (\boldsymbol{r} - \boldsymbol{r}_i)/h_i$: $u = a + bx + cy + dx^2 + exy + fy^2$, where a, b c, d, e and f are constants. A little algebra shows that, at the location of particle i, then $u = u_i$:

$$u_i = \frac{\langle u\sigma\rangle_i\langle\sigma r^4\rangle_i - \langle u\sigma r^2\rangle_i\langle\sigma r^2\rangle_i}{\langle\sigma\rangle_i\langle\sigma r^4\rangle_i - \langle\sigma r^2\rangle_i^2}, \tag{C.1}$$

where $r = |\boldsymbol{r} - \boldsymbol{r}_i|$ and for any quantity q

$$\langle q\sigma\rangle_i \equiv \sum_j m_j q_j W_{ij}. \tag{C.2}$$

Now in practice we only know the actual particle velocities, $\dot{\boldsymbol{r}}_i$, but these can be substituted into the right-hand-side of this equation to give an estimate of the smoothed velocity field at the particle location, $\boldsymbol{u}_i$:

$$\boldsymbol{u}_i = \frac{\langle\dot{\boldsymbol{r}}\sigma\rangle_i\langle\sigma r^4\rangle_i - \langle\dot{\boldsymbol{r}}\sigma r^2\rangle_i\langle\sigma r^2\rangle_i}{\langle\sigma\rangle_i\langle\sigma r^4\rangle_i - \langle\sigma r^2\rangle_i^2}, \tag{C.3}$$

Figure C.10 shows the raw and smoothed particle speeds in the x-direction near the hydraulic jump shown in Figure 4. As can be seen, the value of u is smoother than that of the raw data, as expected, and in particular tends to smooth out the velocity peaks. Even in this extreme situation, u is well-behaved.

The damping is implemented via an extra pair-wise acceleration (once again, preserving conservation of momentum)

$$\ddot{\boldsymbol{r}}_i \leftarrow \ddot{\boldsymbol{r}}_i + \sum_j m_j \left[\frac{\boldsymbol{a}_i W_{ij}}{\sigma_i} - \frac{\boldsymbol{a}_j W_{ji}}{\sigma_j}\right], \tag{C.4}$$

where $\boldsymbol{a}_i = (\boldsymbol{u}_i - \dot{\boldsymbol{r}}_i)/(C_{\rm damp}\Delta t)$. Here $C_{\rm damp}$ is a damping coefficient and Δt is the timestep. For linear damping, we use the same expression but replace $\boldsymbol{u}_i$ with $\langle\sigma\dot{\boldsymbol{r}}_i\rangle$.

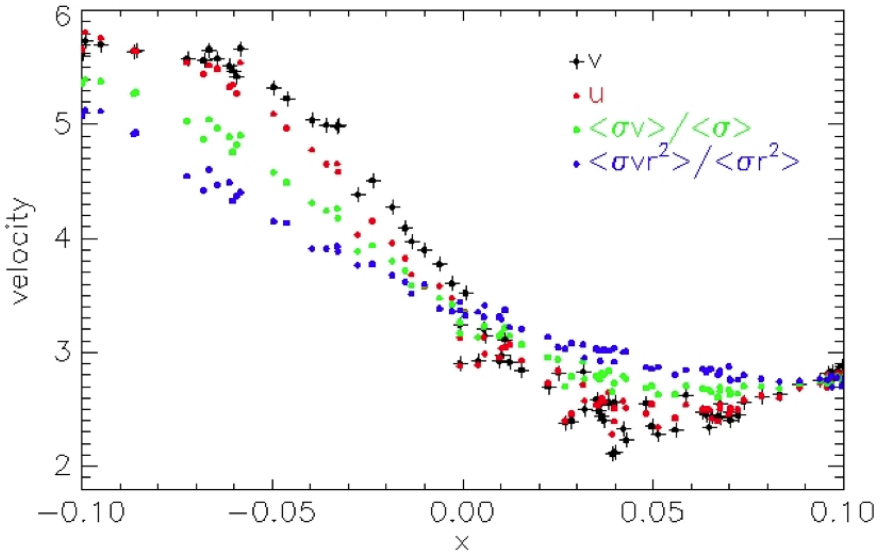

Figure C.10: This figure shows the raw and smoothed particle speeds in the x-direction near the hydraulic jump shown in Figure 4: black, v, - raw particle speeds; red, u, - the smoothed expression given in Equation C.3; green - the density-weighted mean speed; blue - the density-weighted speed times r^2. The smoothing length of the particles at $x = 0$ is 0.14, i.e. larger than the region shown on the plot, and samples just 24 neighbours.

Note:

- For irregular particle distributions, then the denominator of Equation C.3 could vanish, leading to numerical instability. In practice, we have not come across situations where this seems to be an issue. As a safeguard, however, we revert to linear damping whenever the denominator is less than 0.1 times $\langle \sigma r^2 \rangle_i^2$.

- Equation C.1 could also be written as follows:

$$u_i = \frac{\langle u \rangle_i \langle r^4 \rangle_i - \langle u r^2 \rangle_i \langle r^2 \rangle_i}{\langle 1 \rangle_i \langle r^4 \rangle_i - \langle r^2 \rangle_i^2}, \tag{C.5}$$

  in which the denominator would appear to be independent of u. However, it would be a mistake (which we made) to think that the denominator can be replaced by the exact value of the corresponding integral: unless the numerator and denominator are sampled at particle locations in the same way, then the approximation will be a poor one.

Appendix D. Benchmark EA3: details

Here we provide more details for the UK Environment Agency benchmark test number 3 that was described in Section 4.1.

The test specification states that a grid cell of 5 m should be used. Because of the way that we set up our initial particle distribution (by creating a glass-like particle distribution within a period square) it was convenient for us to use a particle density of 32 particles per $(5\,\mathrm{m})^2$. With our fiducial value of $N_{\mathrm{SPH}} = 24$ particles within the smoothing kernel, this gave us a slightly higher resolution than specified. The total number of particles in the simulation was 6980.

Figure D.11 shows the volumetric influx of water across the inlet at $x = 0$ as a function of time. The initial momentum of the water is not specified.

Figure D.12 shows the required outputs for the EA3 test: the water surface height at $x = 150$ & $250\,\mathrm{m}$, and the mean water velocity in the x-direction at those locations, as a function of time. In the upper-left panel, the scale has been greatly exaggerated so as to show the difference between three different choices of damping. This can make a significant difference to the measured height of the water while it is sloshing back and forth, but the difference in the final water depth is smaller and lies within the main band of results returned by the other codes that participated in the test.

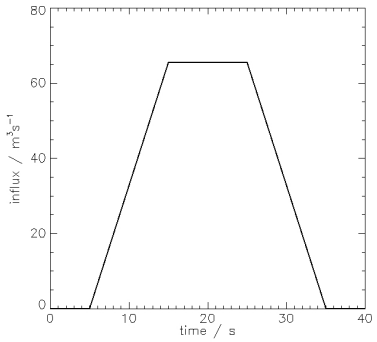

Figure D.11: The volumetric influx of water in test EA3 as a function of time.

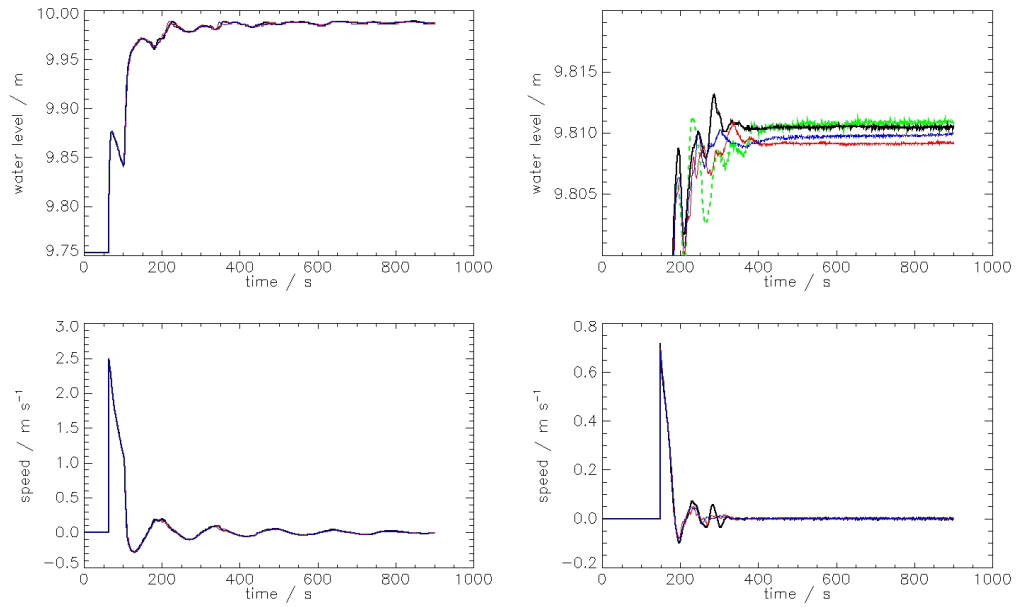

Figure D.12: Test EA3: top – water surface height at $x = 150\,\mathrm{m}$ (left) & $x = 250\,\mathrm{m}$ (right); bottom – mean water velocity in the x-direction at $x = 150\,\mathrm{m}$ (left) & $x = 250\,\mathrm{m}$ (right). Three different damping schemes are shown: black – quadratic, $C_{\mathrm{damp}} = 1$; red – quadratic, $C_{\mathrm{damp}} = 10$; blue – linear, $C_{\mathrm{damp}} = 3$. The dashed, green line has the same damping parameters as the black one, but shows the effect of reducing the particle resolution.

The dashed green line shows a run with the same damping parameters as the black one, but with a lower resolution of 20.5 particles per $(5\,\mathrm{m})^2$. That again leads to rather different behaviour in the oscillating part of the flow, but to a final height that is similar to the higher-resolution case.

Our fiducial run (the black curve in the figures) ran for 2248 steps and took 115 s of CPU on a MacBook Pro with a 2.3 GHz Intel 4-Core i7 processor. We used the gfortran/gcc-4 compiler with optimisation level -O2.

References

[1] R. A. Gingold, J. J. Monaghan, Smoothed particle hydrodynamics - Theory and application to non-spherical stars, MNRAS 181 (1977) 375–389.

[2] L. B. Lucy, A numerical approach to the testing of the fission hypothesis, Astronomical Journal 82 (1977) 1013–1024.

[3] M. Rodriguez-Paz, J. Bonet, A corrected smooth particle hydrodynamcis formulation of the shallow-water equations, Computers and Structures 83 (2005) 1396–1410.

[4] A. Panizzo, D. Longo, P. De Girolamo, Tsunami early warning system. part 3: Sph modelling of nlswe, Proceedings of the XXXth Convegno di Idraulica e Construzioni Idrauliche, Rome, Italy (2006).

[5] M. de Leffe, D. Le Touze, B. Alessandrini, Sph modeling of shallow-water coastal flows, Journal of Hydraulic Research 48 (2010) 118–125.

[6] R. Vacondio, B. D. Rogers, P. K. Stansby, P. Mignosa, Sph modeling of shallow flow with open boundaries for practical flood simulation, Journal of Hydraulic Engineering (2011).

[7] T.-J. Chang, H.-M. Kao, M.-H. Hsu, Numerical simulation of shallow-water dam break flows in open channels using smoothed particle hydrodynamics, Journal of Hydrology 408 (2011) 78–90.

[8] M. Pastor, B. Haddad, G. Sorbino, S. Cuomo, V. Drempetic, A depth integrated, coupled sph model for flow-like landslides and related phenomena, Int. J. Numer. Anal. Mech. Geomech. 33 (2009) 143–172.

[9] R. Vacondio, B. D. Rogers, P. K. Stansby, Smoothed particle hydrodynamics: Approximate zero-consistent 2-d boundary conditions and still shallow-water tests, Int. J. Numer. Meth. Fluids 69 (2012) 226–253.

[10] R. Vacondio, B. D. Rogers, P. K. Stansby, Accurate particle splitting for smoothed particle hydrodynamics in shallow water with shock capturing, International Journal for Numerical Methods in Fluids (2011).

[11] R. Vacondio, B. D. Rogers, P. K. Stansby, P. Mignosa, Shallow water sph for flooding with fynamic particle coalescing and splitting, Advances in Water Resources 58 (2013) 10–23.

[12] R. Vacondio, B. D. Rogers, P. K. Stansby, P. Mignosa, A correction for balancing discontinuous bed slopes in two-dimensional smoothed particle hydrodynamics shallow water modeling, Int. J. Numer. Meth. Fluids (2012) n/a.

[13] H. Lee, S. Han, Solving the shallow water equations using 2d sph particles for interactive applications, Vis Comput 26 (2010) 865–872.

[14] S. Néelz, G. Pender, Benchmarking the latest generation of 2D hydraulic modelling packages, Report SC120002, Environment Agency, Horison House, Deanery Road, Bristol, BS1 9AH, 2013.

[15] V. Springel, L. Hernquist, Cosmological smoothed particle hydrodynamics simulations: the entropy equation, MNRAS 333 (2002) 649–664.

[16] S. Soares-Frazão, Y. Zech, Dambreak flow experiment: the isolated building test case., EC Research Project EVG1-CT2001-0037 WP3 Flood Propagation, IMPACT (Investigation of Extreme Flood Processes and Uncertainty), Available from: http://www.impact-project.net/wp3_technical.htm [Accessed 28 March 2014], 2002.